Article:

Incompressible SPH Simulation of Solitary Wave Interaction with Movable Seawalls

Dongfang Liang[1,2], Wei Jian[3], Songdong Shao[4,5,*], Ridong Chen[6] and Kejun Yang[7]

[1] Department of Engineering, University of Cambridge, Cambridge CB2 1PZ, UK. Email: dl359@cam.ac.uk

[2] Collaborative Innovation Centre for Advanced Ship and Deep-Sea Exploration (CISSE), Shanghai 200240, P.R. China.

[3] Maritime Institute, Nanyang Technological University, 50 Nanyang Avenue, Singapore 639798. Email: jianwei@ntu.edu.sg

[4*] Department of Civil and Structural Engineering, University of Sheffield, Sheffield S1 3JD, UK. Email: s.shao@sheffield.ac.uk (Correspondence author)

[5] State Key Laboratory of Hydro-Science and Engineering, Tsinghua University, Beijing 100084, P.R. China

[6] State Key Laboratory of Hydraulics and Mountain River Engineering, Sichuan University, Chengdu 610065, P.R. China. Email: chenridong1984@163.com

[7] State Key Laboratory of Hydraulics and Mountain River Engineering, Sichuan University, Chengdu 610065, P.R. China. Email: yangkejun@163.com

Abstract

In this paper, we applied an incompressible Smoothed Particle Hydrodynamics (SPH) method to investigate the impact of solitary waves on seawalls, especially movable seawalls. The SPH method is a mesh-free numerical approach particularly suitable for dealing with large free surface deformations and complex fluid-structure interactions. The incompressible SPH (ISPH) method solves the pressure field using the pressure Poisson equation (PPE), rather than relying on the equation of state. It has the advantage of producing more stable and accurate pressure fields and impact forces on structures. We first applied the model to simulate the solitary wave propagation and runup against a fixed vertical wall. The computations compared well with previous experimental and numerical results. Then, the solitary wave impact on a movable structure was investigated by replacing the fixed wall with a spring-controlled seawall subject to different spring stiffness and mass settings. Particular attention was paid to the prediction of the seawall movement, wave runup height and hydrodynamic loading. The incident wave height was found to be the dominant factor for the movable seawall movement during and immediately after the wave crest arrival at the seawall. Other factors, such as the seawall mass and spring stiffness, become important to the seawall's responses only after the maximum impact.

Introduction

Free-surface flow problems in hydrodynamics are of great interest to engineers due to their industrial and environmental importance. Most of the free-surface flows involve strong dynamics and large surface deformations, which makes it more challenging in analysing these flows. Among the various free-surface flows, the interaction between waves and man-made structures are of particular interest to the designers of offshore structures and coastal defences. There are a large number of factors that contribute to the wave propagation and subsequent breaking and impact on the structures near-shore. Analytical solutions may be available only for some simple geometries and idealized flow conditions. With the fast advancement of computer technology, it becomes increasingly crucial for numerical tools to efficiently and accurately model the behaviour of these flows.

The Smoothed Particle Hydrodynamics (SPH) method, is an emerging computational tool for free-surface flows. Being a Lagrangian method, it naturally deals with the free surface breaking and water fragmentation. Monaghan (1994) first extended the SPH application from astrophysics to incompressible flows with a free surface. A weakly compressible assumption was made in modelling water flows to avoid any computational complication. It has since been used in a wide range of free-surface flow applications, such as dam-break flooding (Liang, 2010; Pu et al., 2013), wave propagating near shore (Dalrymple and Rogers, 2006), interfacial flows (Colagrossi and Landrini, 2003; Grenier et al., 2013) and fluid-solid interactions (Khayyer et al., 2009; Liang et al., 2010; Canelas et al., 2016).

The conventional weakly-compressible SPH (WCSPH) method has been found to suffer from nonphysical pressure fluctuations near solid boundaries which is mainly caused by the amplification of small density errors through the equation of state. A common practise for WCSPH users to palliate this drawback is to calculate forces based on acceleration instead of pressure. To fully overcome the aforementioned drawback, incompressible SPH (ISPH) models had been developed in the past decade, based on some early works on another popular mesh-free method, Moving Particle Semi-implicit (MPS), e.g. Koshizuka et al. (1998), Gotoh and Sakai (1999), and

3

Hwang et al. (2014). The basic principle of the ISPH approach is that the fluid pressure is solved by a pressure Poisson equation (PPE) based on a strict incompressibility condition. Some pioneering ISPH research had been carried out by Cummins and Rudman (1999) and Shao and Lo (2003). The computational cost for solving the PPE in ISPH is much larger than that of the WCSPH, but the ISPH model allows a time step much larger than the WCSPH method (Zheng et al., 2014).

The SPH study on the wave interaction with offshore structures is a very active research area in hydrodynamics and coastal engineering. It has been heavily used in the field of wave propagation and wave-structure interactions (Gómez-Gesteira and Dalrymple, 2004; Crespo et al., 2007; Rogers et al., 2010; Barreiro et al, 2013; Altomare et al., 2014; Altomare et al., 2015; Ren et al., 2015; Lin et al., 2015). Readers are referred to Gómez-Gesteira et al. (2010) for an overview of the various research outcomes. So far, most of the coastal structures studied are fixed objects and very little research has been conducted on movable coastal structures. In engineering practice, allowing some degree of flexibility in structures could improve the performance of coastal defence and reduce the construction cost. For example, Pimanmas et al. (2010) proposed a conceptual design for tsunami shelters to be constructed with energy-absorbing connectors which can be modelled as spring elements to withstand large debris impact.

In this paper, an extensive study on the solitary wave propagation and impact on a coastal seawall in both fixed and mobile conditions is carried out. The wave runup height and hydrodynamic loading on the vertical walls are examined in details. The ISPH model used in this study follows the divergence-free-velocity-field ISPH algorithm (Lee et al., 2008) with corrected formulation for the Laplacian operator proposed by Schwaiger (2008). The new formulation has been found to provide good pressure stability and accuracy near boundaries. The ISPH model is validated by simulating a solitary wave impact on a fixed vertical seawall, followed by applications on a passively moving seawall. The analysis concentrates on the dependence of wave runup height, seawall movement and hydrodynamic loading on the incident wave and seawall characteristics.

SPH Methodology and Implementation

SPH principle and formulation

The SPH formulations are based on the concept of integral interpolations. By using a kernel function to describe the connectivity of discrete particles, the differential operators in the Navier-Stokes equations can be approximated by the summations over particles. Each particle carries information about the velocity, density, mass, pressure and other flow variables.

For a function $f(\mathbf{r})$ that represents a physical variable over a domain of interest, where $\mathbf{r}$ is the position vector, its discrete notation is approximated by the values on particles within a compact support. The function $f(\mathbf{r})$ at particle i can be written as a summation over all its neighbouring particles j as follows,

$$f(\mathbf{r}_i) \approx \sum_j \frac{m_j}{\rho_j} f(\mathbf{r}_j) W_{ij} \tag{1}$$

where m_j, ρ_j are the mass and density of particle j, respectively; and W_{ij} is the kernel function that denotes $W(|\mathbf{r}_i - \mathbf{r}_j|, h)$, where h is the smoothing length related to the size of the compact support. The kernel function W determines how the variables are interpolated and smoothed over the particles. The kernel function that has been widely used by SPH practitioners is the cubic spline kernel function. The smoothing length h determines the size of the stencil in spatial discretization. In practice, it is common to use a smoothing length $h = 1.0 \sim 1.3\,\Delta r$, where Δr corresponds to the initial particle spacing.

The particle approximation of the spatial derivative of a function, such as the pressure gradient, can be written as,

$$\frac{1}{\rho_i} \nabla P_i = \sum_j m_j \left(\frac{P_i}{\rho_i^2} + \frac{P_j}{\rho_j^2} \right) \nabla_i W_{ij} \tag{2}$$

where P is the pressure and $\nabla_i W_{ij}$ is the gradient of the kernel taken with respect to particle i. There are two approaches for calculating the viscosity. One is to introduce an artificial viscosity to provide necessary dissipations of the kinetic energy and

prevent unphysical particle penetrations. The other is to simulate the physical viscosity, which is used in the present paper as,

$$\nu \nabla^2 \mathbf{v}_i \approx \sum_j m_j \frac{\rho_i \nu_i + \rho_j \nu_j}{\rho_i \rho_j} \frac{\mathbf{r}_{ij} \cdot \nabla_i W_{ij}}{\mathbf{r}_{ij}^2 + \eta^2} \mathbf{v}_{ij} \tag{3}$$

where ν is the viscosity coefficient of the fluid, $\mathbf{v}$ is the velocity vector, $\mathbf{r}_{ij} = \mathbf{r}_i - \mathbf{r}_j$ and $\mathbf{v}_{ij} = \mathbf{v}_i - \mathbf{v}_j$ and η is a small value to prevent singularity.

The second-order derivative of the kernel function is often used to model the Laplacian operator in the ISPH approach. The exact discretisation of the Laplacian operator may cause a distinct pressure decoupling pattern due to the double summations in the formulation (Cummins and Rudman, 1999). Similar to the treatment of viscosity in Eq. (3), an approximate projection method for the Laplacian operator has been adopted in the ISPH model,

$$\nabla \cdot \left(\frac{1}{\rho} \nabla P \right)_i \approx \frac{2}{\rho_j^2} \sum_j m_j \frac{\mathbf{r}_{ij} \cdot \nabla_i W_{ij}}{\mathbf{r}_{ij}^2 + \eta^2} P_{ij} \tag{4}$$

where $P_{ij} = P_i - P_j$.

Governing equations and ISPH solution methods

The governing equations for modelling an incompressible fluid in the discretised form are as follows,

$$\nabla \cdot \mathbf{v} = \mathbf{0} \tag{5}$$

$$\frac{d\mathbf{v}}{dt} = -\frac{1}{\rho} \nabla P + \nu \nabla^2 \mathbf{v} + \mathbf{g} \tag{6}$$

where $\mathbf{g}$ is the gravitational acceleration.

The ISPH method couples the pressure and velocity fields implicitly, which is different from the conventional WCSPH approach. The momentum equation (Eq. (6)) is solved in two steps. In the predictor step, an intermediate velocity field $\mathbf{v}^*$ is calculated with only the viscous and gravitational terms. This step is explicit in time and the incompressibility requirement is not considered.

$$\mathbf{v}_i^* = \mathbf{v}_i^n + \left(\nu \nabla^2 \mathbf{v}_i^n + \mathbf{g} \right) \Delta t \tag{7}$$

where Δt is the time step. Superscripts n and * represent the previous and intermediate time steps, respectively. The particle position at the intermediate time step is updated as

$$\mathbf{r}_i^* = \mathbf{r}_i^n + \mathbf{v}_i^* \Delta t \tag{8}$$

The incompressibility requirement is then enforced at the corrector step. The velocity at the next time step, $\mathbf{v}_i^{n+1}$, can be calculated from the intermediate velocity, $\mathbf{v}_i^*$, and the pressure field obtained from the pressure Poisson equation (PPE) as

$$\mathbf{v}_i^{n+1} = \mathbf{v}_i^* - \left(\frac{1}{\rho} \nabla P^{n+1} \right)_i \Delta t \tag{9}$$

The particle positions at the new time step (n+1) are updated as

$$\mathbf{r}_i^{n+1} = \mathbf{r}_i^n + \left(\mathbf{v}_i^{n+1} + \mathbf{v}_i^n \right) \frac{\Delta t}{2} \tag{10}$$

The intermediate velocity $\mathbf{v}_i^*$ is projected onto a divergence-free velocity field. Taking the divergence of Eq. (9) and combining with Eq. (5) gives

$$\nabla \cdot \left(\frac{1}{\rho} \nabla P^{n+1} \right)_i = \frac{1}{\Delta t} \nabla \cdot \mathbf{v}_i^* \tag{11}$$

where the source term on the right-hand side is the divergence of the intermediate velocity field. It can be written in the SPH form as,

$$\nabla \cdot \mathbf{v}_i^* \approx \sum_j \frac{m_j}{\rho_j} \left(\mathbf{v}_j^* - \mathbf{v}_i^* \right) \cdot \nabla_i W_{ij} \tag{12}$$

Initial and boundary conditions

The fluid particles are initially placed on an equidistant rectangular grid. The pressure and velocity are set to zero at t = 0.00 s. All particles have the same constant density and mass.

The flow domain is bounded by two types of boundaries: solid boundaries and free surfaces. On the solid boundaries, the non-penetration condition is imposed. The dummy particle method (Koshizuka et al., 1998; Gotoh and Sakai, 1999) is used here due to its simple implementation and satisfactory performance. Two types of the boundary conditions also exist at the free surface, i.e. kinematic and dynamic boundary conditions. The kinematic boundary condition requires that the fluid

elements at the free surface remain on it throughout the flow movement. This is automatically satisfied by the Lagrangian nature of the SPH method. Assuming the surface tension is negligible and the viscous coefficient is very small, the dynamic boundary states the atmospheric pressure at the surface. The surface particles need to be identified, whose pressure is then set to zero before solving the PPE in the ISPH method. In this paper, the surface particles are identified by calculating the divergence of the particle positions at the intermediate time level (Lee et al., 2008):

$$\nabla \cdot \mathbf{r} = \sum_{j} \frac{m_j}{\rho_j} \mathbf{r}_{ij} \cdot \nabla_i W_{ij} \tag{13}$$

For inner fluid particles with full kernel support, the position divergence should be equal to 2.0 in two-dimensional applications. The surface particles that have truncated kernel support will have a much smaller divergence values than those of inner particles. The common practice of using 1.5 as the threshold value is followed in this study.

Application I - Solitary Wave Impact on Fixed Seawalls

The aim of this section is to validate the ISPH model for its ability to simulate solitary wave runup and impact on a fixed vertical wall. The numerical examples considered in the study are idealised to be two-dimensional. The solitary waves are considered for its close resemblance to tsunami wave characteristics. This example was previously studied using the MAC method (Chan and Street, 1970), WCSPH method (Monaghan and Kos, 1999) and MPS method (Gotoh et al., 2005).


Model setup

The numerical water tank is 2.5 m long with a uniform mean water depth of 0.20 m. The solitary wave is generated by the paddle movement at the left-end of the tank. The piston-type wavemaker following Goring (1978) is adopted in generating solitary waves of different amplitudes. The main computational parameters used in the ISPH model are: particle spacing $\Delta r = 0.008$ m and time step $\Delta t = 0.001$ s. The generated solitary wave arrives at the fixed wall on the right-end of the tank and is subsequently reflected back within 4.0 s in all the cases conducted.

Results and discussions

Surface profiles

Several wave ratios have been considered to study the wavemaker movement and wave propagation over time. One simulation case with a large wave amplitude, A = 0.10 m, is detailed herein to demonstrate the ability of ISPH model to study strong wave nonlinearity. Fig. 1 presents a series of particle configurations after the initiation of the paddle movement. The surface profile at t = 1.00 s shows that a water column of approximately 0.30 m high has already formed in front of the wave paddle. By t = 1.30 s the established waveform has travelled to x = 0.80 m at a wave elevation of 0.10 m. The maximum runup at the downstream seawall takes place at t = 2.40 s with a height of 0.27 m in front the wall. The pressure profiles demonstrate accurate incompressible enforcement as very little pressure fluctuation can be observed near the solid boundaries even with such a large incident wave height.
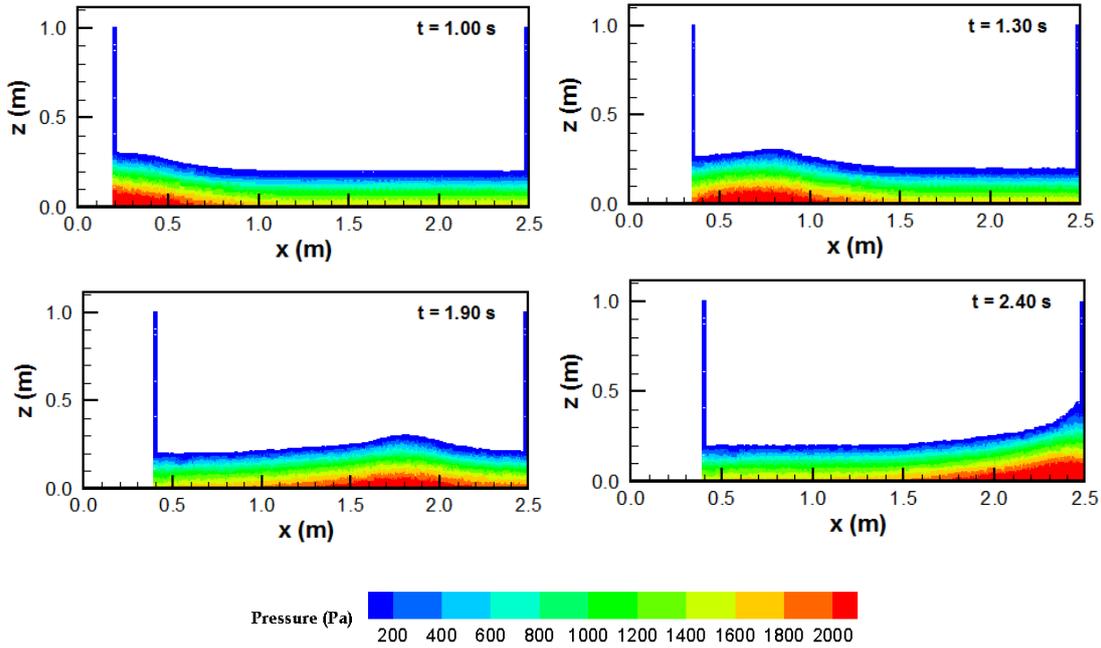
Fig. 1. Snapshots of surface profiles with pressure contours at t = 1.00 s, 1.30 s, 1.90 s and 2.40 s for wave ratio H/h = 0.5.

The wave surface profiles at time t = 1.60 s and 1.89 s are compared with the first-order solitary wave solutions in Fig. 2. A good agreement in the free-surface profiles

has been found, especially at the wave front. The large discrepancy at the tail of the wave will gradually decrease as the wave propagates away from the wavemaker. Figs. 1 and 2 also suggest that the pressure distributions generally follow the hydrostatic law, which is consistent with the long wave nature of the solitary wave.
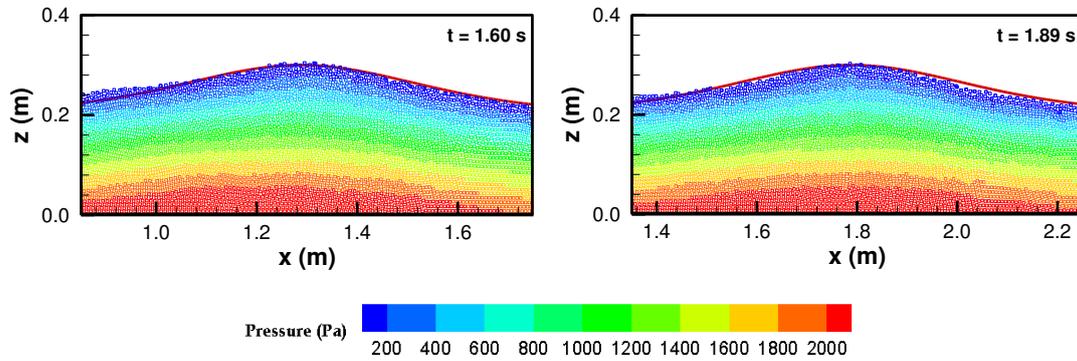
Fig. 2. Free-surface profiles comparing the ISPH results with solitary wave analytical solutions (in red solid line) at t = 1.60 s (left) and 1.89 s (right).

Wave runup height

The maximum wave runup height in front of the vertical wall has been examined for a number of height-to-depth ratios, H/h, ranging from 0.1 to 0.6. Fig. 3 compares the ISPH predictions with numerous published experimental and numerical data. The simulated results from the ISPH model are shown to agree well with the published data. It is shown that higher incident waves tend to generate a larger runup at the vertical wall. Owing to the wave nonlinearity, the correlation is not a straight line.
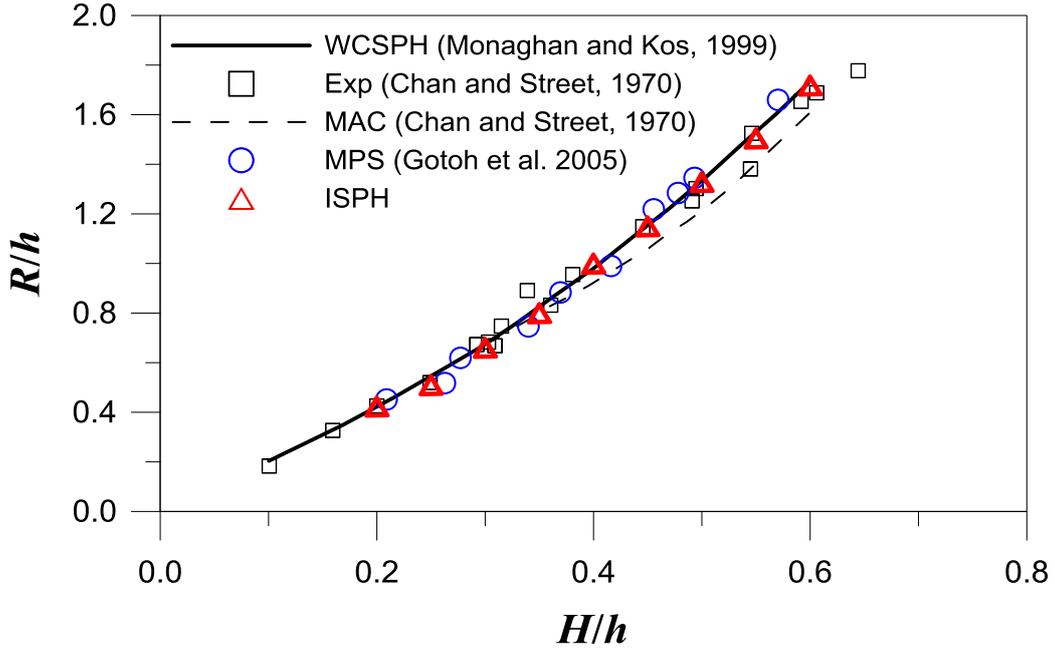
Fig. 3. Maximum wave runup for different height-to-depth ratios.

Hydrodynamic loading on the wall

The wave impact force exerted on the vertical seawall is investigated in this section. In the SPH model, the forces experienced by any solid bodies can be evaluated by integrating the surface stress over the volume of the boundary particle domain. Since the pressure component of the stress tensor always dominates the hydrodynamic loading for wave colliding with solid bodies, the following formulation is adopted to evaluate the impact force on vertical walls. The viscous component of the stress tensor is assumed to be negligible when compared with the pressure term.

$$F_{impact} = m_i \cdot \sum_j \frac{m_j}{\rho_j} \left[-\left(\frac{P_j}{\rho_j} + \frac{P_i}{\rho_i} \right) \right] \cdot \nabla_i W_{ij} \tag{14}$$

To verify this equation, the pressure force acting on the vertical wall of the water tank is computed under hydrostatic condition using the ISPH formulation. Fig. 4 shows the non-dimensional force experienced by the wall computed by the ISPH model for water depths ranging from 0.2 m to 0.4 m over 1.0 s. The impact force computed by Eq. (14) is non-dimensionalized as follows,

$$F^* = F_{impact} / F_{static} \tag{15}$$

where F^* is the non-dimensional impact force and F_{static} denotes the hydrostatic force on the wall. It can be seen that the force experienced by the solid wall can be correctly estimated. Some small oscillations can be observed before t = 0.30 s, which are

11

caused by the initial adjustment of fluid particles near solid boundaries. All particles were assigned zero velocity and zero pressure at t = 0.0 s, so it takes time to establish the correct hydrostatic condition. The intensity of the fluctuation increases with water depth, but these initial disturbances settle down very quickly as time elapses.
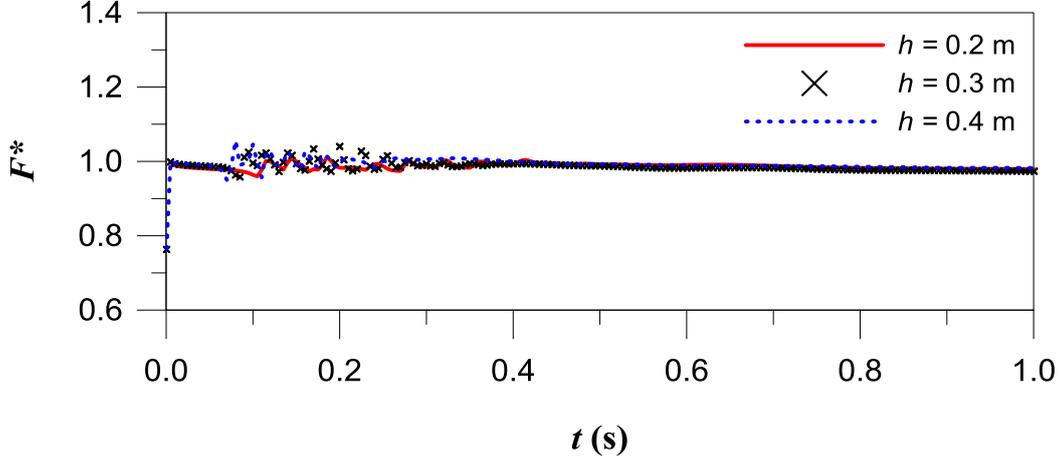
Fig. 4. Non-dimensional impact force on the water tank wall by ISPH model at different water depths.

After the hydrostatic test, we apply Eq. (14) to estimate the dynamic forces induced by the collision of solitary wave on a vertical wall. Cooker et al. (1997) used a boundary-integral method to study this phenomenon, which will be used as a reference in the comparison. Six wave height to water depth ratios have been studied, ranging from 0.1 to 0.6. The results are shown in Fig. 5(a) for smaller wave heights H/h = 0.1 to 0.3, and in Fig. 5(b) for larger wave heights H/h = 0.4 to 0.6. In the figure, t_0 denotes the instant of maximum wave runup and $\tau = 1/(h/g)^{1/2}$ is used to normalize the time. The ISPH-computed magnitude of the force history shows a satisfactory agreement with the published numerical results. It can be seen that the forces experienced by the solid wall exhibit very different characteristics depending on the incident wave height. For H/h < 0.4, there exists only one single peak value, which takes place at approximately the same time as the maximum runup. This changes to a double maxima pattern at larger wave heights. The first peak occurs before the maximum runup and the second one takes place afterwards. The same observation has also been reported in Grilli and Svendsen (1990), Cooker et al. (1997) and Shao (2005).

12
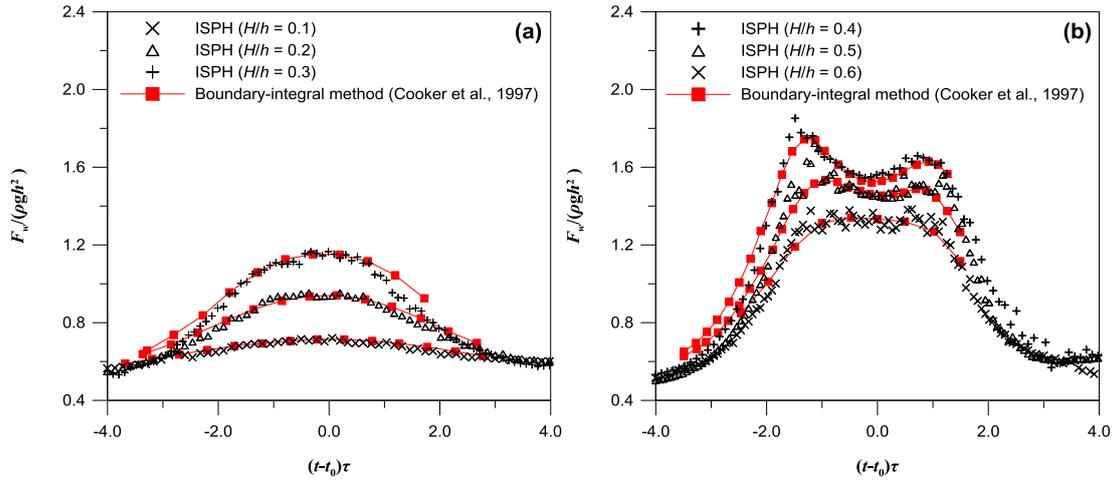
Fig. 5. Solitary wave forces for different wave height-to-depth ratios computed by ISPH and Cooker et al. (1997). (a) H/h = 0.1 ~ 0.3; (b) H/h = 0.4 ~ 0.6.

## Application II - Solitary Wave Impact on Movable Seawalls

Fixed seawalls tend to incur large impact forces and require expensive maintenance over time since they are not able to absorb wave energy. In this section, the wave-structure interactions associated with a passively moving seawall are investigated using the ISPH model. The model of movable seawall is derived from the conceptual design of energy-absorbing tsunami shelters presented in Pimanmas et al. (2010). As a preliminary investigation, it is assumed that the energy-absorbing connectors behave like an ideal spring. In this simplified model, there are only two parameters to describe the properties of the movable structure: seawall mass and spring stiffness. A wide range of spring stiffness and seawall mass values were simulated to understand the behaviour of seawall under different properties. For each combination of the wave height and seawall mass, the value of the spring stiffness spans over a very large range, so that the seawall response becomes insensitive to the stiffness at two extreme situations (very soft spring and very stiff spring). The parametric studies provide a wide range of seawall responses, which is useful in identifying the desired behaviour for design purposes.

Movable seawall model setup

The passively moving seawall is idealized into a simple spring-mass system, which

consists of a spring attached to a vertical wall. Fig. 6 illustrates the numerical geometry of the vertical seawall and spring system. When subject to wave impact, the seawall is able to reduce the hydrodynamic loading by compressing the spring. The energy stored in the compressed spring can be gradually released back into the water by the release of the spring after the wave impact.

The seawall is initially located at $x^0_{seawall} = 2.50$ m under hydrostatic condition, and the spring system is in its relaxed form. As the wave generated by the wavemaker propagates downstream, the seawall will become mobile once the impact force exceeds a specified threshold value. It is assumed that the spring cannot be stretched. As a result, the seawall cannot travel further upstream beyond its initial position.
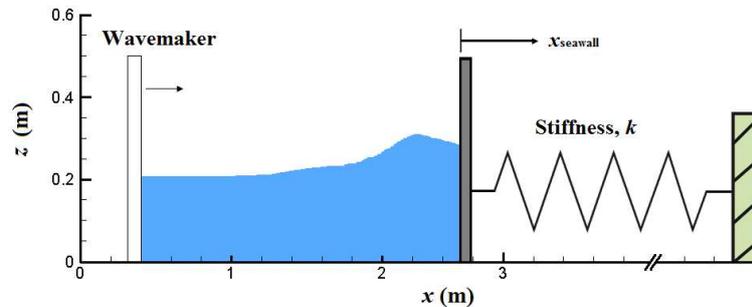
Fig. 6. Schematic sketch of the movable seawall model.

To increase the computational stability, the spring-mass system is designed to sustain a certain amount of impact force before it can be compressed. The onset of motion for the system is determined by a threshold force ratio, defined as $F_{threshold} = 1.10 \times F_{static}$ in this study. Fig. 7 illustrates how this threshold condition compares with the force experienced by the seawall under the impact from a wave height-to-depth ratio H/h = 0.5.
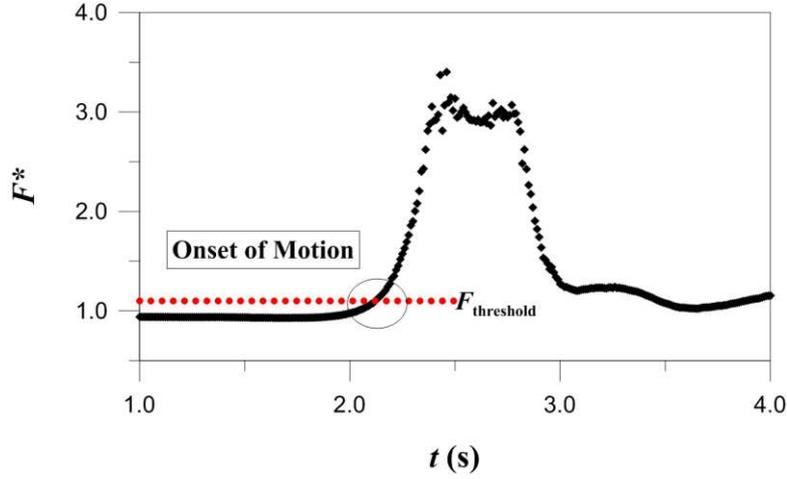
Fig. 7. Illustration of onset motion for the spring-mass system.

Once the seawall becomes mobile, its movement can be determined by a simple free-body force analysis on the seawall. The acceleration, velocity and position of the seawall are calculated as follows,

$$a_{seawall} = \begin{cases} \dfrac{\left(F_{impact} - F_{threshold}\right) - k \cdot \left(x_{seawall} - x_{seawall}^0\right)}{m_{seawall}}, & F_{impact} > F_{threshold} \\ \\ -\dfrac{k \cdot \left(x_{seawall} - x_{seawall}^0\right)}{m_{seawall}}, & F_{impact} \leq F_{threshold} \end{cases} \tag{16}$$

$$v_{seawall}^{n+1} = v_{seawall}^n + a_{seawall}\Delta t \tag{17}$$

$$x_{seawall}^{n+1} = \begin{cases} x_{seawall}^n + v_{seawall}^{n+1}\Delta t, & x_{seawall}^{n+1} > x_{seawall}^0 \\ x_{seawall}^0, & x_{seawall}^{n+1} \leq x_{seawall}^0 \end{cases} \tag{18}$$

where k is the spring stiffness coefficient, $m_{seawall}$ is the mass of seawall, superscripts n and (n + 1) denote the current and next time step.

Computational parameters

The numerical setup in the fixed-wall study is adopted in this section, except that the vertical seawall on the right-hand side is movable. Based on the outcome of the fixed-wall study, a total simulation time of 4.00 s is used. This is considered to be long

15

enough to capture the impact of the solitary wave and the subsequent response of the seawall. The ISPH model used a particle spacing of $\Delta r = 0.008$ m and a time step $\Delta t = 5.0 \times 10^{-4}$ s.

Several contributing factors that influence the seawall movement are examined to understand the underlying physics. It is expected that the seawall movement will be determined by the interaction of incident wave ratio H/h, the spring coefficient k and mass of the seawall $m_{seawall}$. A number of simulations are conducted to investigate the influence of each parameter on the seawall response. Table 1 summarises the values used for the parametric study. Three key computational results are focused in the simulations: the seawall displacement, wave runup height in front of the seawall and the impact force experienced by the seawall.

Table 1 List of values used for the parametric study of movable seawall.

Parameters	Values
Wave height ratio, H/h	0.2, 0.3, 0.4, 0.5, 0.6
Spring coefficient, k (N/m)	0.01, 10, 50, 100, 500, 10^3, 10^4, 10^5, 10^6, 10^7
Seawall mass, $m_{seawall}$ (kg/m)	50, 100, 175, 250, 375, 500

Results and discussions

In this section, we first illustrate the water surface evolution and the movement of the spring-mass system under the impact of a solitary wave. This is followed by an investigation of the individual influence of the three factors listed in Table 1. Lastly, a section summarising their comprehensive effects on the maximum impact force, seawall displacement and runup height measures is presented.

Illustration of seawall responses

The test case illustrated herein has the following wave condition and seawall properties: wave ratio H/h = 0.5, seawall mass $m_{seawall}$ = 250 kg/m and spring stiffness coefficients k = 10 N/m. Fig. 8 presents some snapshots of the surface profiles with pressure contours computed by the ISPH model.

It is observed that the seawall becomes mobile after t = 2.00 s as the wave crest arrives at approximately less than 0.50 m upstream. As the wave crest gradually arrives at the seawall, it pushes the seawall to move downstream, as show in the snapshot at t = 2.20 s. Upon the wave collision with the seawall at t = 2.40 s, it is expected that the spring-mass system will absorb some of the impact through the compression of spring. The residual impact that cannot be absorbed will be reflected by the seawall, sending a wave propagating upstream. This phenomenon is observed in snapshot at t = 2.80 s. Comparing the surface profiles t = 2.40 s and t = 2.80 s, the crest height of the reflected wave is approximately 0.1 m less than the impact wave experienced at the seawall. After the reflected wave crest moves further away from the seawall, it exerts less influence on its behaviour. In this case, due to the small stiffness coefficients, the spring system is not able to provide enough resistance to stop the seawall from moving further downstream. The seawall location is at about 2.95 m at t = 4.00 s, with the reflected wave reaching the wavemaker and generating a runup of approximately 0.07 m in height. Fig. 9 compares the wave force, seawall displacement and wave runup at the seawall with the fixed seawall case. The seawall displacement and wave runup height are non-dimensionalized as follows,
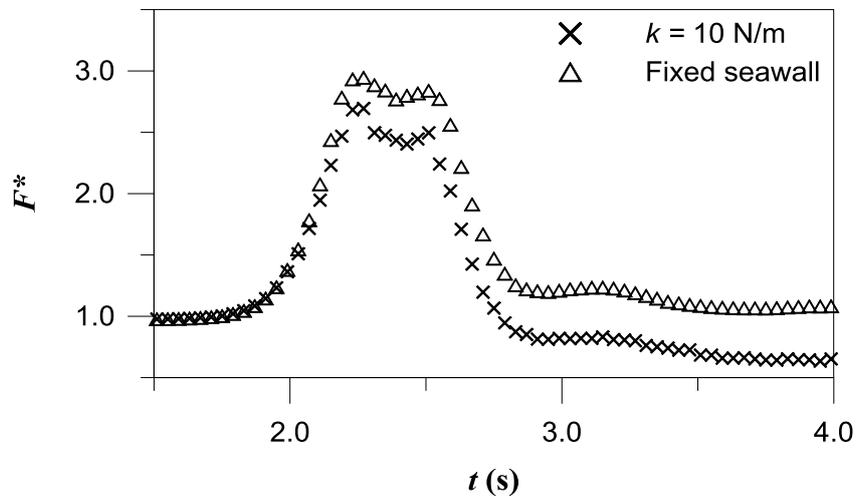
$$x^* = X/h \tag{19}$$

$$R^* = R/h$$
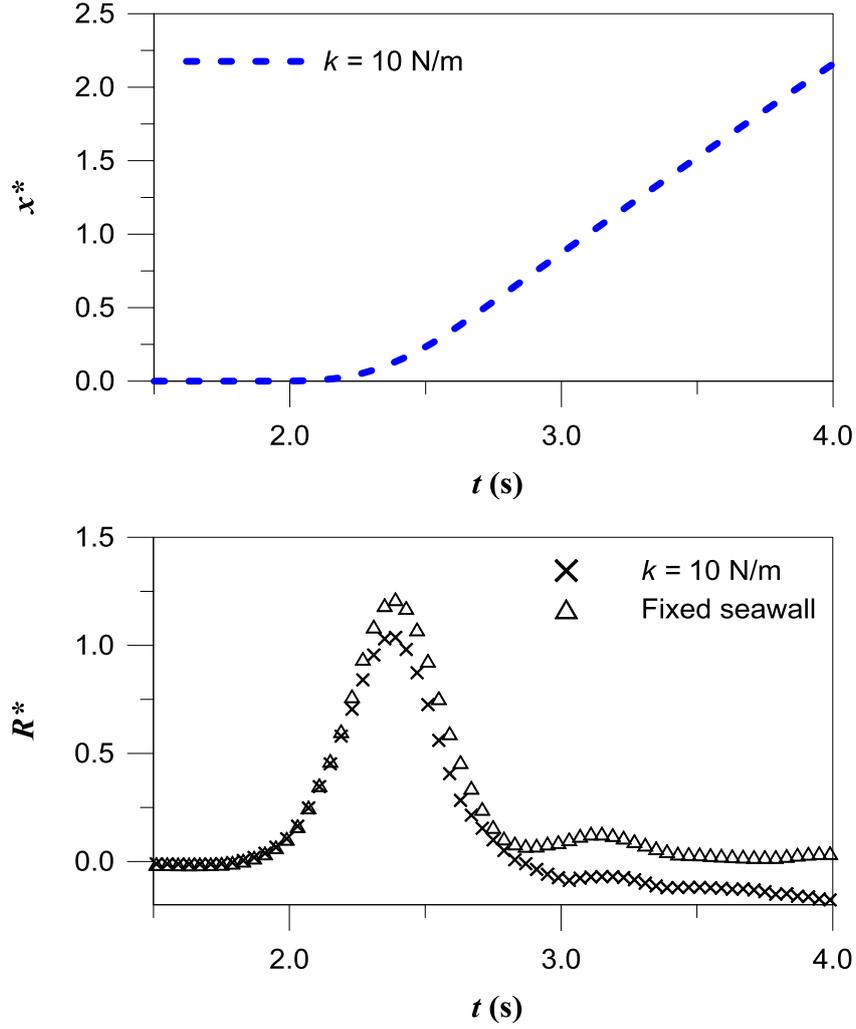
where X denotes the seawall displacement and R the wave runup height.
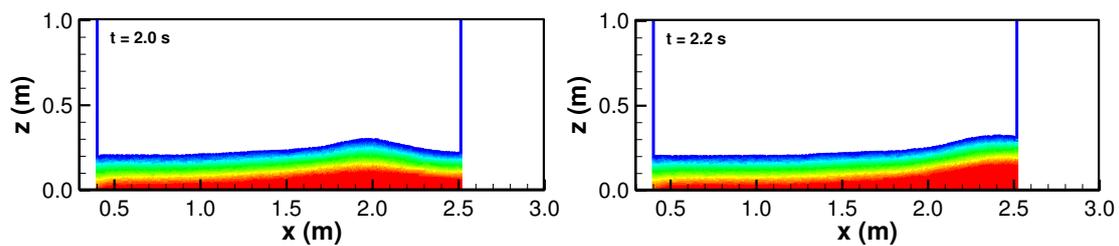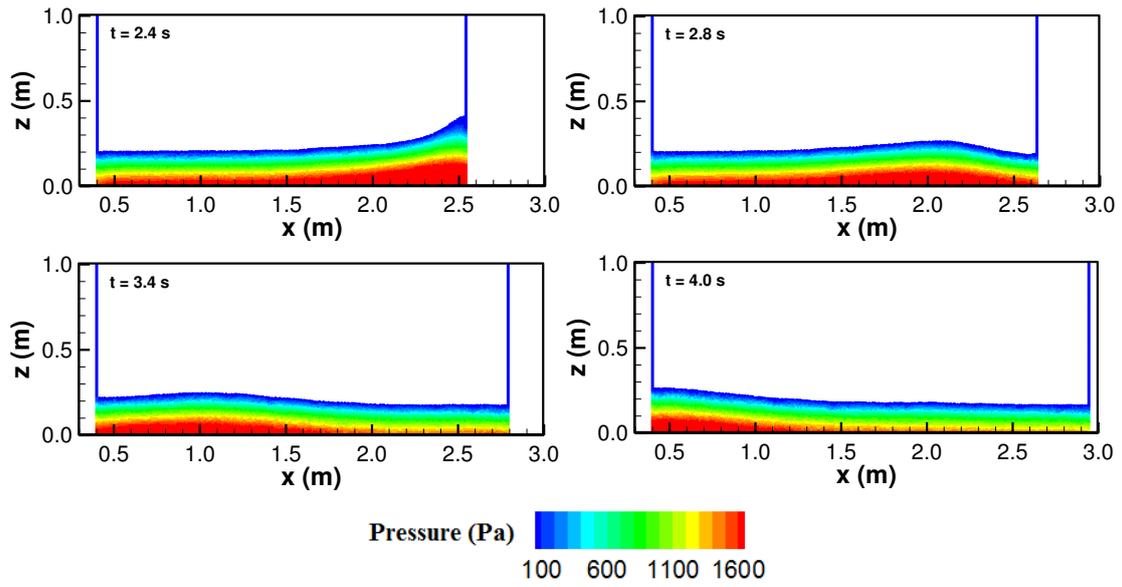
Fig. 8. Wave surface profiles for wave ratio H/h = 0.5, spring stiffness k = 10 N/m and seawall mass $m_{seawall}$ = 250 kg/m.

Fig. 9. Comparison of the non-dimensional impact force (top), seawall displacement (middle) and wave runup height (bottom) for wave ratio H/h = 0.5, seawall mass m$_{seawall}$ = 250 kg/m and spring stiffness k = 10 N/m with fixed seawall scenario.

Similar to the observation from the surface profiles, the impact force experienced by the seawall exceeds the threshold condition at t = 2.00 s and a gradual rise can be seen in the displacement profile after this instant. The force and runup profiles increase rapidly after t = 2.00 s, indicating the approaching of wave crest. The impact force reaches the maximum at t = 2.24 s with a magnitude of 2.73×F$_{static}$, which is approximately 8.72% less than the peak impact force experienced by the fixed seawall. This is followed by the peak runup occurrence at t = 2.40 s with a magnitude of 1.04×h, again less than the maximum runup of 1.21×h under fixed scenario. By t = 2.90 s, the impact force has dropped to below the static level for the flexible seawall, which explains the dominance of spring properties beyond this time instant. The seawall continues to move downstream at a constant speed after t = 2.90 s, further

compressing the spring system. This causes the impact force and runup at the seawall to decrease further. At t = 4.00 s, the seawall is at 2.16×h downstream of its original place. The water level in front of the seawall is 0.18×h below its initial mean water depth, which leads to a pressure force of 0.63×F_{static}. This test case demonstrates that by allowing some flexibility in the seawall, the peak force and runup experienced during the wave impact can be reduced accordingly.

Spring stiffness effect

To fully understand the seawall behaviour under different spring stiffness, Fig. 10 compares the non-dimensional impact force, seawall displacement and runup height at the seawall from eight different stiffness coefficients for $m_{seawall}$ = 50 kg/m and H/h = 0.3. It is obvious that the seawall response can be grouped into three categories.

For very flexible spring system with k ≤ 10 N/m, the spring system gets compressed continuously throughout the computation and offers little or no resistance to slow down the seawall movement downstream. As a result, the impact force and runup height experienced by the seawall under this setting are much smaller, with the maximum impact force at 1.70×F_{static} and peak runup at 0.50×h upon wave impact. The total displacement of the seawalls at t = 4.00 s has increased the computational domain by one third of its original length, which leads to the impact force and runup height fall below the static condition.
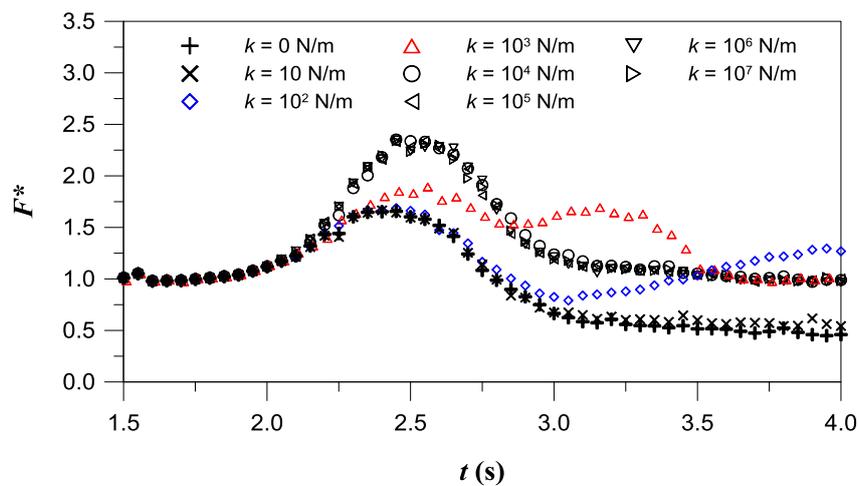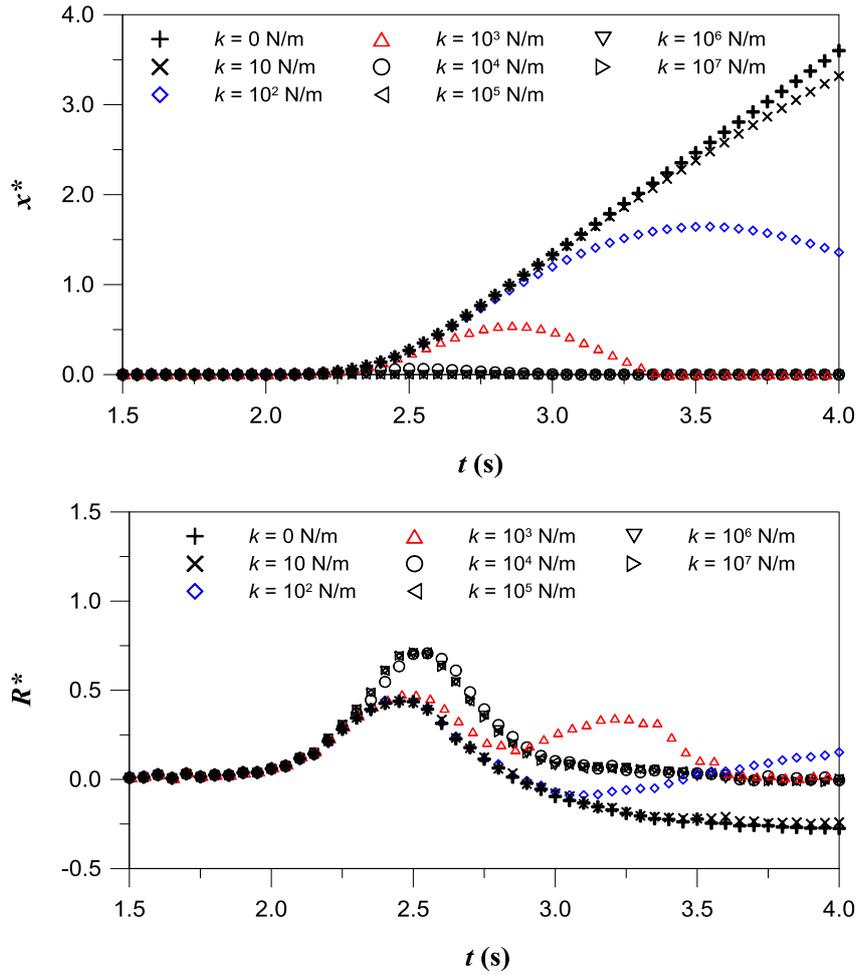
Fig. 10. Time histories of impact force (top), seawall displacement (middle) and wave runup height (bottom) for different spring stiffness coefficients.

On the other end of the stiffness spectrum, the seawalls behaved very similar to a fixed seawall for $k \geq 10^4$ N/m. The displacement profiles remain zero or nearly zero for seawalls fall in this category. The maximum impact force is $2.40 \times F_{static}$ and the peak runup height is $0.75 \times h$, both increased by approximately 50% from the seawalls with $k \leq 10$ N/m. The force and runup height at $t = 4.00$ s returned to 1.0 and 0.0, respectively.

The transition state ranges from $k = 10^2$ N/m to 10^4 N/m, where we see the seawall incurs some displacement downstream upon the first collision with wave crest arrival but the spring system manages to reverse the movement of seawall as time elapses. For the seawall with $k = 10^2$ N/m, it behaved very similar to seawalls with smaller stiffness values up until $t = 2.80$ s when the impact force experienced by the seawall falls back to the static condition. The force profile starts to deviate from the more

flexible seawalls and its displacement curve starts to slow down. A maximum displacement of 1.64×h takes place at approximately t = 3.50 s, after which the seawall gradually moves towards its original place, driving the force and runup profiles rise significantly during the slow-down and restoration process. At t = 4.00 s, the seawall is located at 1.36×h downstream from its initial position. Both force and runup height at the seawall are significantly larger than the static conditions. Whilst for the seawall with k = 10^3 N/m, the spring system managed to restore the seawall to its original place. The force and runup height profiles rise slightly higher at the initial impact, and the seawall exhibited more resistance towards the impact force. Twin peaks were observed in the corresponding force and runup height profiles, first peak corresponds to the collision with the wave crest arrival and second peak takes place when the seawall returns to its original place. A maximum displacement of 0.55×h occurs at t = 2.88 s, when the force and runup height are at their localized minima after the first peak. The seawall behaves like a fixed seawall after t = 3.50 s, soon after it returns to the original place.

In general, the spring stiffness determines the seawall response during the wave crest arrival and after it moves away from the close proximity of the seawall. Very flexible spring system offers very little resistance towards the residual impact and by the continuous compression of spring it allows a significant reduction in the maximum force and runup height at the seawall at the time of impact. Whilst very stiff spring makes the seawall virtually a fixed object and no wave absorption takes place. The transition range (10^2 N/m ≤ k ≤ 10^4 N/m) is where the seawall behaviour is less predictable. Depending on the relative strength of the incident wave and spring system, the maximum impact force and runup height are reduced accordingly by allowing some seawall movement. However, some temporary rise in the impact force and runup height at the seawall will occur during the restoring movement of seawall. A seawall with spring stiffness close to the upper limit of the transition (k ~ 10^4 N/m) tends to cause a higher rise due to the quick release of the compressed spring within a short period of time.

Seawall mass effect

In addition to the spring stiffness, the self-weight of the seawall can also affect the response since mass is inversely proportional to the acceleration. In this section, six

different seawall mass values are assigned to the flexible seawall and studied under a spring stiffness k = 500 N/m and wave condition, H/h = 0.5. The comparison of the non-dimensional impact force, seawall displacement and wave runup height are shown in Fig. 11.

As expected, the force and runup height profiles exhibit very similar trend among the seawall with different weights when the wave impact dominates the near-field interaction before t = 2.80 s. The maximum impact force and runup height due to the wave crest arrival increases with increasing mass values, since heavier seawalls are expected to offer more resistance to moving and behave more like fixed seawalls. It can be observed that there is very little to no difference in the response from seawalls with $m_{seawall} \geq 375$ kg/m. The maximum impact force is approximately $2.90 \times F_{static}$. For seawalls with $m_{seawall} \leq 250$ kg/m, the force and runup profiles are more spread-out and show varying degrees of absorption of impact wave upon encountering the incident wave crest. The maximum impact force ratios for $m_{seawall} = 50 - 250$ kg/m are 2.10, 2.40, 2.60 and 2.70, respectively. This suggests that there exists a threshold mass value beyond which the seawall resembles a fixed seawall.

23
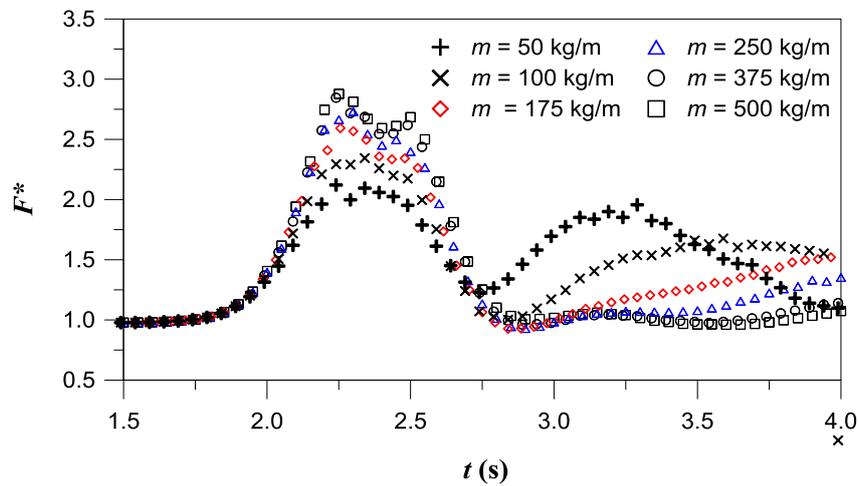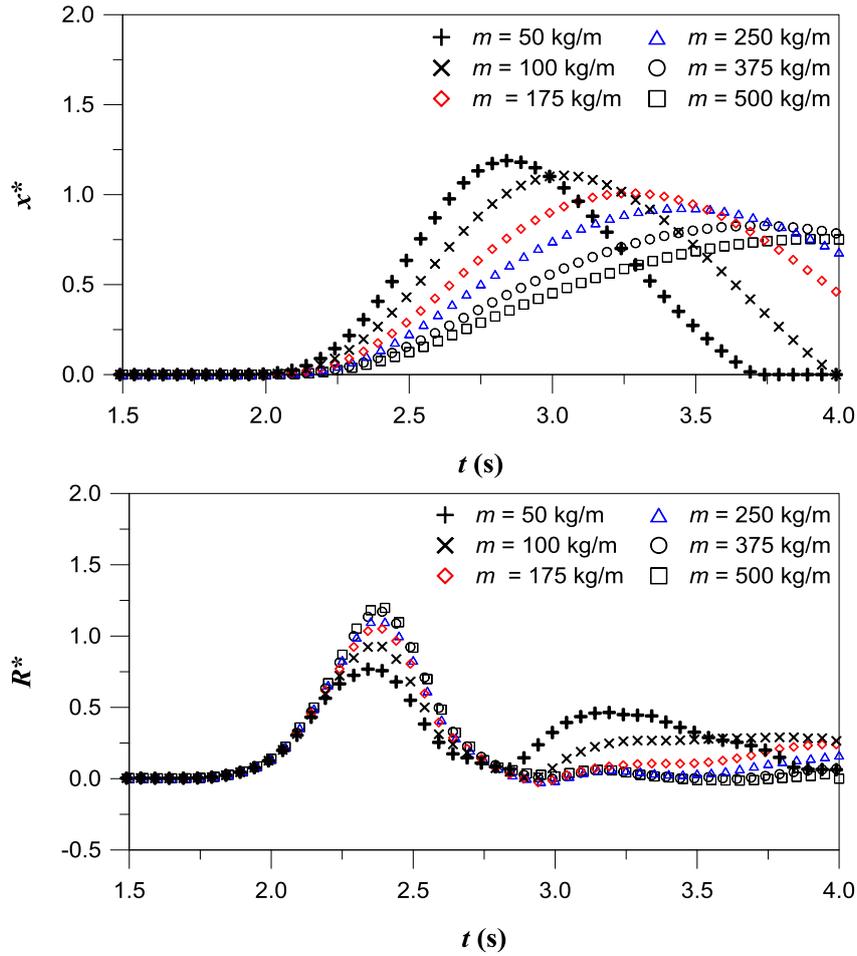
Fig. 11. Time histories of wave force ratio (top), seawall displacement (middle) and wave runup height (bottom) for different seawall mass values.

A second rise in the impact loading and runup height can be observed for seawalls with $m_{seawall} \leq 250$ kg/m, which is caused by the returning seawall. The magnitude and rate of this rise is inversely correlated to the seawall mass, heavier seawalls are less prone to generate a large water accumulation when subject to the release of the compressed spring. This is confirmed in the displacement profiles, in which as the seawall mass increases the displacement curve becomes more smoothed out. The energy stored in the compressed spring is released at a slower rate into the flow domain, causing a more subtle disturbance to the flow.

In general, the impact loading and runup height at the seawall is positively correlated to the seawall mass upon the arrival of the incident wave crest. Heavier seawalls tend to generate a higher impact force and runup until a threshold mass value is reached

beyond which the seawall behaviour closely resembles a fixed one. When the near-field interaction becomes dominated by the spring system, the impact loading and runup height caused by the restoring seawall is negatively correlated to the seawall mass. Lighter seawalls are more prone to cause a large amount of runup and impact loading due to larger acceleration.

Wave height to water depth ratio effect

The previous two sections examined the influence of seawall properties on the impact loading and runup height experience at the seawall, which is dominate at some time after the arrival of wave crest at the seawall. In this section, the strength of the incident wave is studied to understand its effect on the seawall response during the early stage of the impact. Five different wave ratios are simulated, ranging from H/h = 0.2 to 0.6. Fig. 12 shows the impact force, seawall displacement and runup height for these wave ratios with a spring stiffness k = 500 N/m and seawall mass $m_{seawall}$ = 250 kg/m.

The profiles suggest that, under the same spring flexibility and seawall mass, the wave height determines both the arrival time of the incident wave at the seawall and the maximum impact force. The higher the wave ratio is, the earlier the force profile rises up to its maximum. This is also reflected in the wave runup and seawall displacement profiles, with respect to the time instant at which the water height rises and the seawall initiates its movement. The displacement profiles suggest that the onset of the seawall starts at approximately t = 2.00 s, 2.08 s, 2.12 s, 2.20 s and 2.32 s as the wave ratios decreases from 0.6 to 0.2. The wave impact force ratio reaches a maximum value of 3.21, 2.71, 2.38, 2.10 and 1.72 at t = 2.20 s, 2.30 s, 2.43 s, 2.48 s and 2.58 s for seawalls subject to decreasing wave ratios. This corresponds to the occurrence of peak runup at t = 2.35 s, 2.38 s, 2.43 s, 2.51 s and 2.62 s with a ratio of 1.54, 1.12, 0.83, 0.60 and 0.38, respectively. Large wave impacts tend to generate a faster build-up of water in front of the seawall, which is shown in the steepness of the slopes in the force and runup profiles. Same trend is observed in the retreating stage of both profiles between t = 2.50 s and 3.00 s.
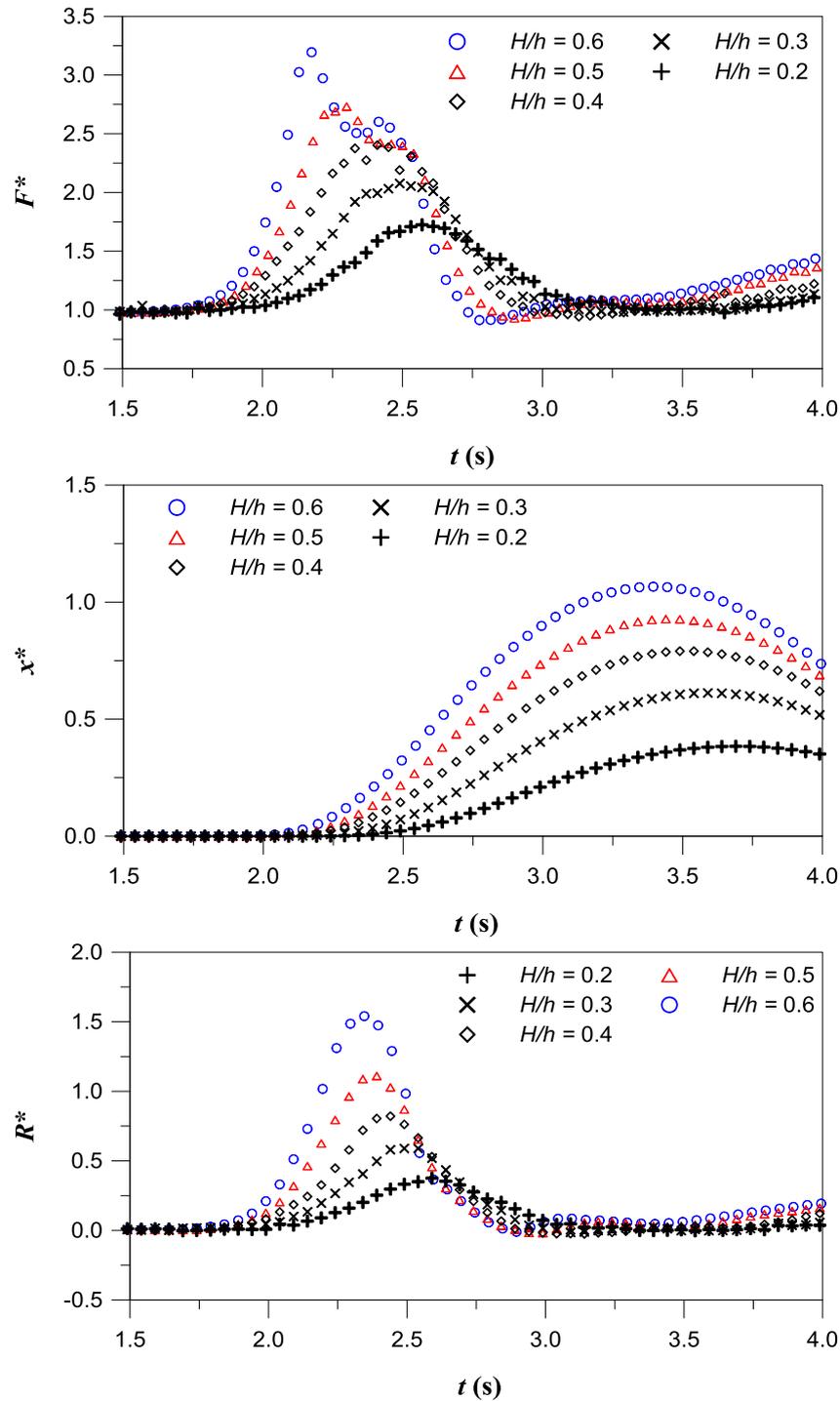
Fig. 12. Time histories of wave force ratio (top), seawall displacement (middle) and wave runup height (bottom) for different incident wave ratios.

The impact force and runup height profiles after t = 3.00 s show very little difference in seawall response. This is expected since by this time the reflected wave has moved further away from the seawall, exerting less influence in the near-field interaction. The seawall response is mainly determined by the seawall property and its relative

strength to the residual wave loading near the seawall. It is noticed that seawalls under larger incident tend to generate a slightly higher runup upon its movement towards its original position. Since the seawall subject to larger wave impact stored more energy through the compressed spring at the encounter, it is expected to release more energy back into the flow domain upon the restoration of the seawall. The difference in the amount of this second rise in the impact force and runup height among different incident wave height is much smaller in scale when compared to the first rise.

Collective effects

In this section, the dependence of the maximum wave impact force, seawall displacement and wave runup height on the three key parameters, incident wave height, spring stiffness and seawall mass, is investigated and summarised. In order to generalize our findings, the following three groups of non-dimensional parameters are used to represent the incident wave characteristics and seawall properties.

$$H / h \tag{20}$$

$$k^* = k / \rho h^2 g$$

$$m^*_{seawall} = m_{seawall} / \rho h^2$$

Fig. 13 plots the maximum seawall displacements against the spring coefficients on a semi-logarithmic scale. Regardless of the incident wave ratio and seawall mass, the displacement decreases with the increasing spring stiffness. This decrease is more apparent for larger incident waves and lighter seawall. The curves generally demonstrate that for any given seawall mass and incident wave height, the seawall response shows very little variations when $\log(k^*) < -1.59$, where the spring system undergoes continuous compression under the dominance of wave impact loading. As the spring stiffness increases, the displacement decreases quite rapidly over the region $-1.59 \leq \log(k^*) \leq 1.41$. Further increasing the stiffness reduces the magnitude of displacement and all curves virtually return to zero by $\log(k^*) = 2.41$. It is observed that the increment between each curve is almost evenly spaced for any given seawall mass setting, which suggests that the displacement is roughly linearly correlated to the wave ratios. Considering the effect of the seawall mass, it is evident that the maximum displacement at $\log(k^*) \leq -4.0$ reduces with increasing seawall mass. Due to larger inertia and thus smaller seawall movement during the impact, the slopes in

the region between log(k*) = -1.59 and 1.41 are much milder for heavier seawalls.
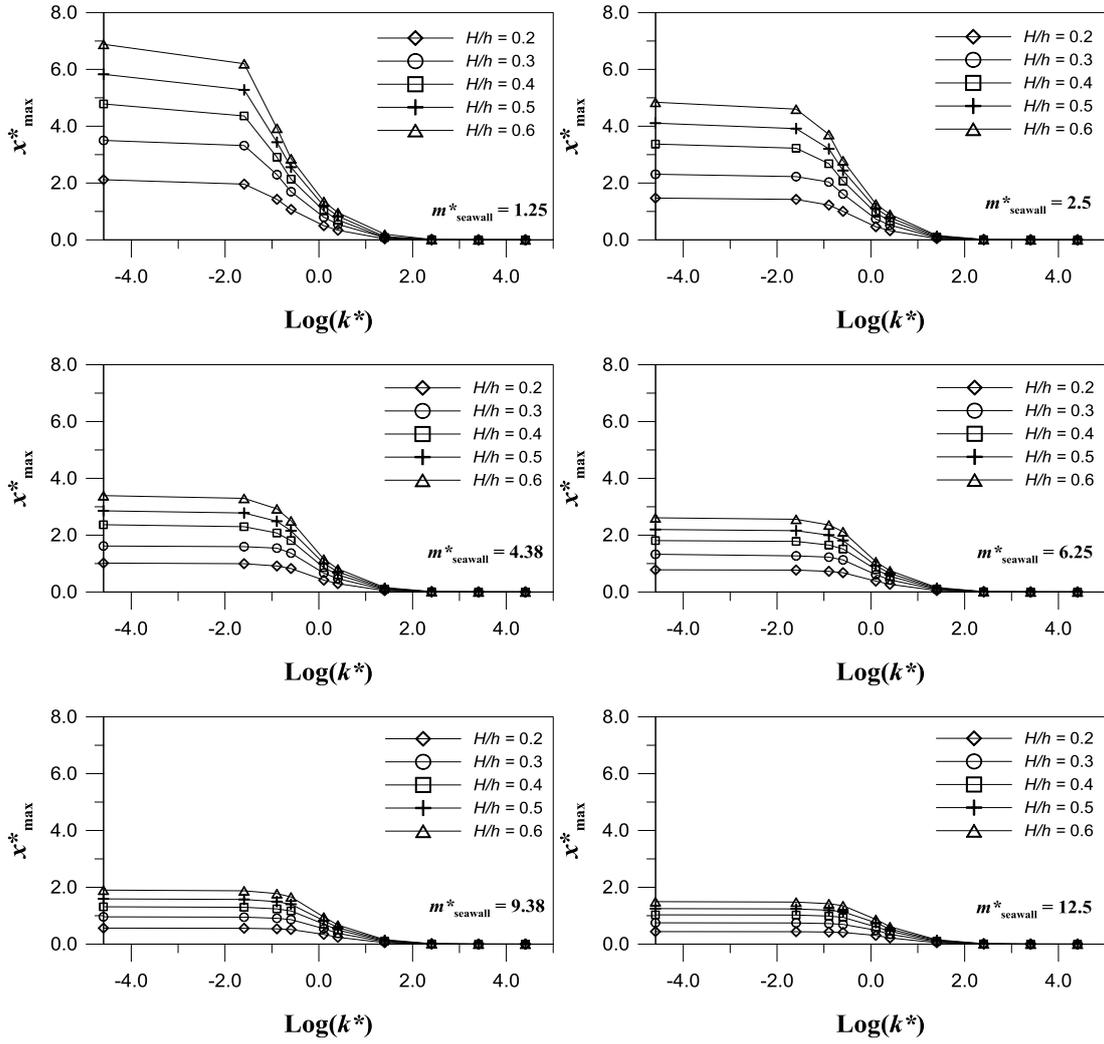

Fig. 13. Maximum seawall displacements versus spring stiffness coefficients for different wave ratios and seawall masses.

Figs. 14 and 15 compare the maximum impact force and runup height against the spring stiffness on semi-logarithmic scales, respectively. Both figures consist of two relatively flat-line regions for log(k*) < 0.41 and log(k*) > 2.41 and an upward-sloped transition zone in between. Lighter seawalls with smaller stiffness coefficients tend to experience less impact force and smaller water runup upon the wave crest arrival. The upward slopes in the transition region steepen up with increasing wave ratio and decreasing seawall mass. For very flexible seawalls, the spring reaction is negligible in relation to the wave impact force. The incident wave intensity and seawall inertia alone determine the seawall reaction. Hence, both the impact force and runup height

are not affected by the spring stiffness for log(k*) < 0.41. Whilst for very large stiffness (log(k*) > 2.41), the seawall behaviour and wave impact phenomenon are similar to those for fixed seawalls. It is expected that when the spring stiffness is sufficiently large, the impact forces and the runup heights at the seawall are dependent on neither the spring stiffness nor the seawall mass; they are only functions of the solitary wave height. For light seawall (m*$_{seawall}$ = 1.25) under a relatively small wave (H/h = 0.2), the runup height increases by only approximately 37.2% from a free-moving seawall (log(k*) < -4.0) to a fixed one (log(k*) > 4.0); whereas when subject to a large wave (H/h = 0.6), the change is around 43.2%. These measures reduce to 6.9% and 7.4% for m*$_{seawall}$ = 12.5, respectively. It is expected that if the mass of the seawall is infinitely large, its own inertia will eventually resist any seawall movement during the impact. The impact force and the runup height profiles will simply be horizontal lines across the whole spring stiffness range.
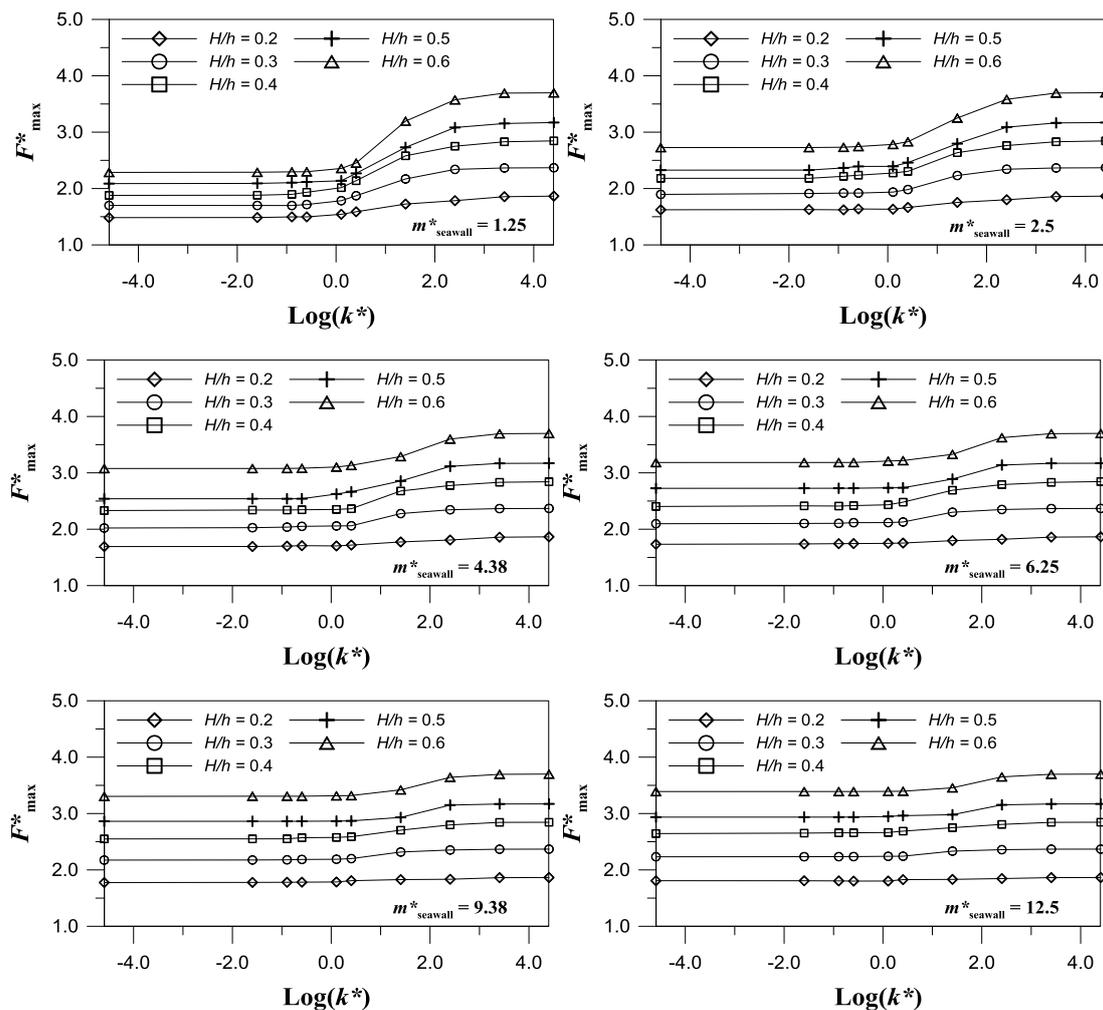
Fig. 14. Maximum wave force ratios versus spring stiffness coefficients for different wave ratios and seawall masses.
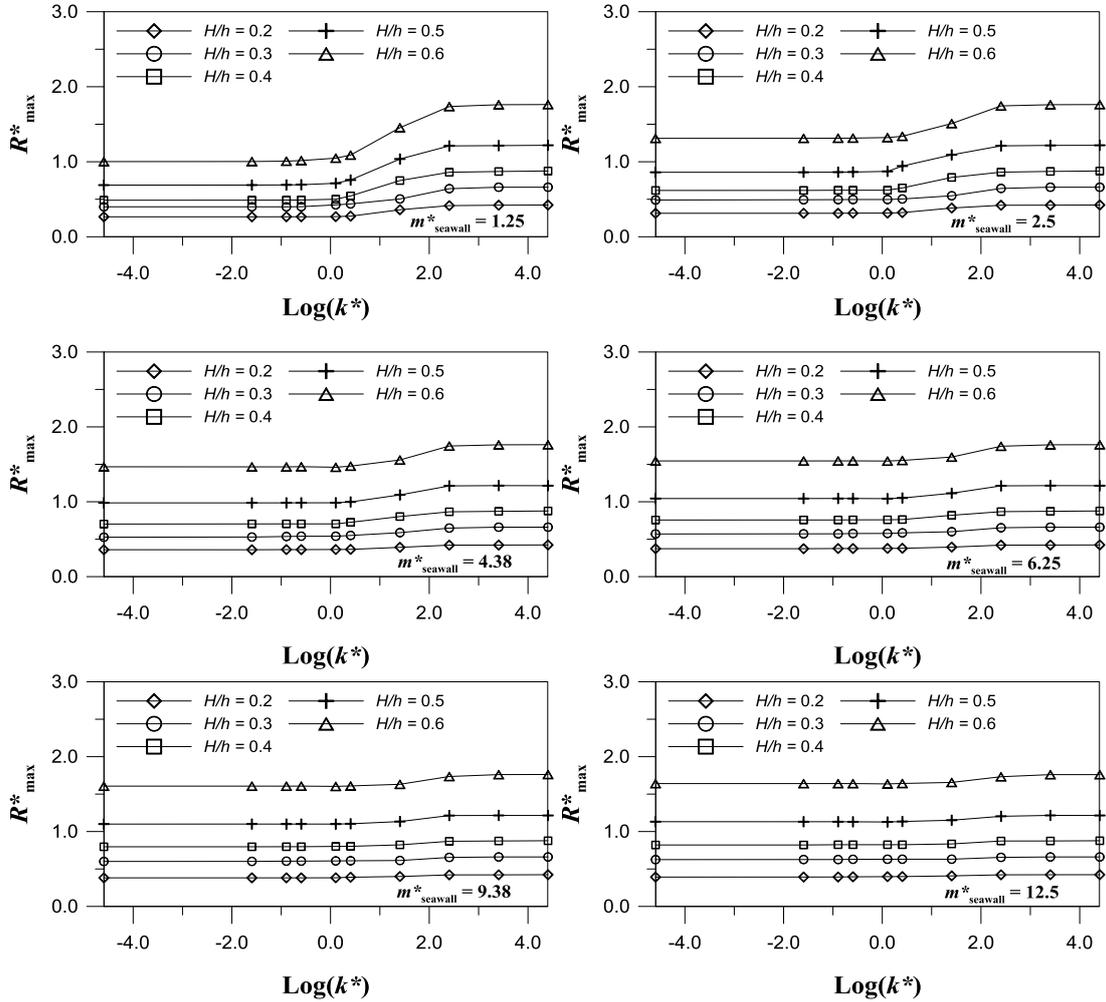
Fig. 15. Maximum wave runup heights versus spring stiffness coefficients for different wave ratios and seawall masses.

Conclusions

This paper explores the application of an incompressible SPH (ISPH) method to wave-structure interaction problems that contain free surfaces and moving solid/water interfaces. The ISPH model has demonstrated to be capable of producing stable and accurate pressure fields. The computed wave runup heights at a fixed vertical seawall agree well with published experimental and numerical results. The ability of the ISPH model in estimating pressure forces on solid boundaries has been examined under

both hydrostatic and hydrodynamic conditions. The estimated force compares well with the theoretical solutions, even for large-amplitude nonlinear waves.

In the movable seawall applications, a spring-mass system subject to solitary wave impact is systematically studied. The movement of the spring-controlled seawall is analysed under the influence of three contributing parameters: incident wave intensity, seawall mass and spring stiffness. The simulation results concentrate on the evaluations of the peak impact force experienced by the seawall, wave runup height and maximum seawall displacement. It has been found that the incident wave amplitude generally dominates the seawall movement during the initial wave impact. It determines the timing and magnitude of the impact force and runup height. Large amplitude waves induce an early arrival of wave crest at the seawall and a large subsequent impact force. The seawall mass and spring stiffness play an important role in determining the seawall response at the stage immediately after the initial impact. Very light and flexible seawalls offer no resistance to the wave loading, which can reduce the collision force and runup heights by moving rapidly downstream upon impact. In practice, such structures can incur large maintenance expenses and prove to be undesirable due to the large seawall displacement and slow restoration phase. On the other hand, very heavy and stiff seawalls virtually behave like fixed seawalls. Between the two aforementioned extremes, the seawall can provide some resistance to the wave attack by incorporating a small degree of flexibility. The present study offers insights into the selection of optimal parameters in the design of movable seawalls and other offshore structures.

The present study considers the seawall to be infinitely long, thus the problem is vertical two-dimensional. Future research may extend to the three-dimensional situation, in which the wave diffraction will be investigated by the movable seawall of a finite length.

Acknowledgements

References

Altomare, C., Crespo, A.J.C., Rogers, B.D., Domínguez, J.M., Gironella, X., Gómez-Gesteira, M. (2014), Numerical modelling of armour block sea breakwater with Smoothed Particle Hydrodynamics, Computers and Structures, 130: 34-45.

Altomare C., Crespo, A.J.C., Domínguez, J.M., Gómez-Gesteira, M., Suzuki, T., Verwaest, T. (2015), Applicability of Smoothed Particle Hydrodynamics for estimation of sea wave impact on coastal structures. Coastal Engineering, 96: 1-12.

Barreiro, A., Crespo, A.J.C., Domínguez, J.M., Gómez-Gesteira, M. (2013), Smoothed Particle Hydrodynamics for coastal engineering problems, Computers and Structures, 120, 96-106.

Canelas R.B., Crespo A.J.C., Domínguez J.M., Ferreira R.M.L., Gómez-Gesteira, M. (2016), SPH-DCDEM model for arbitrary geometries in free surface solid-fluid flows, Computer Physics Communications, 202, 131-140.

Chan, R.K.C., Street, R.L. (1970), A computer study of finite amplitude water waves, Journal of Computational Physics, 6, 68-94.

Colagrossi, A., Landrini, M. (2003), Numerical simulation of interfacial flows by smoothed particle hydrodynamics, Journal of Computational Physics, 191(2), 448-475.

Cooker, M.J., Weidman, P.D., Bale, D.S. (1997), Reflection of a high-amplitude solitary wave at a vertical wall, Journal of Fluid Mechanics, 342, 141-158.

Crespo, A.J.C., Gómez-Gesteira, M., Dalrymple, R.A. (2007), 3D SPH simulation of large waves mitigation with a dike, Journal of Hydraulic Research, 45(5), 631-642.

Cummins, S.J., Rudman, M. (1999), An SPH projection method, Journal of Computational Physics, 152, 584-607.

Dalrymple, R.A., Rogers, B.D. (2006), Numerical modelling of water waves with the SPH method, Coastal Engineering, 53(2-3), 141-147.

Gómez-Gesteira, M., Dalrymple, R.A. (2004), Using a 3D SPH Method for Wave Impact on a Tall Structure, Journal of Waterway, Port, Coastal and Ocean Engineering, 130(2), 63-69.

Gómez-Gesteira, M., Rogers, B.D., Dalrymple, R.A., Crespo, A.J.C. (2010), State-of-art of classical SPH for free-surface flows, Journal of Hydraulic Research, 48, 6-2.

Goring, D.G. (1978), Tsunamis – The Propagation of Long Waves onto a Shelf, Ph.D. Thesis, California Institute of Technology, Pasadena, CA.

Gotoh, H., Sakai, T. (1999), Lagrangian simulation of breaking waves using particle method, Coastal Engineering Journal, 41, 303-326.

Gotoh, H., Ikari, H., Memita, T., Sakai. T. (2005), Lagrangian particle method for simulations of wave overtopping on a vertical seawall, Coastal Engineering Journal, 47,157-181.

Grenier, N., Le Touze, D., Colagrossi, A., Antuono, M., Colicchio, G. (2013), Viscous bubbly flows simulation with an interface SPH model, Ocean Engineering, 69, 88-102.

Grilli, S., Svendsen, I. A. (1990), The propagation and runup of solitary waves on steep slopes, CACR Rep. 91-04, Department of Civil Engineering, University of Delaware.

Hwang, S. C., Khayyer, A., Gotoh, H., Park J. C. (2014), Development of a fully Lagrangian MPS-based coupled method for simulation of fluid-structure interaction problems, Journal of Fluids and Structures, 50, 497-511.

Khayyer, A., Gotoh, H., Shao, S. (2009), Enhanced predictions of wave impact pressure by improved incompressible SPH methods, Applied Ocean Research, 31(2), 111-131.

Koshizuka, S., Nobe, A., Oka, Y. (1998), Numerical analysis of breaking waves using the moving particle semi-implicit method, International Journal for Numerical Methods in Fluids, 26, 751 -769.

Lee, E.-S., Moulinec, C., Xu, R., Violeau, D., Laurence, D., Stansby, P.K. (2008), Comparisons of weakly compressible and truly incompressible algorithms for the SPH mesh free particle method, Journal of Computational Physics, 227, 8417-8436.

Liang, D. (2010), Evaluating shallow water assumptions in dam-break flows, Proceedings of the Institution of Civil Engineers – Water Management, 163(5), 227-237.

Liang, D., Thusyanthan, I., Madabhushi, S.P.G., Tang, H. (2010), Modelling solitary waves and its impact on coastal houses with SPH method, China Ocean Engineering, 24(2), 353-368.

Lin, P., Liu, X., Zhang, J. (2015), The simulation of a landslide-induced surge wave and its overtopping of a dam using a coupled ISPH model, Engineering Applications of Computational Fluid Mechanics, 9(1), 432-444.

Monaghan, J.J. (1994), Simulating free surface flows with SPH, Journal of Computational Physics, 110, 399-406.

Monaghan, J.J., Kos, A. (1999), Solitary waves on a Cretan beach, Journal of Waterway, Port, Coastal and Ocean Engineering, 125(3), 145-154.

Pimanmas, A., Joyklad, P., Warnitchal, P. (2010), Structural design guideline for Tsunami evacuation shelter, Journal of Earthquake and Tsunami, 4(4), 269–284.

Pu, J., Shao, S., Huang, Y., Hussain, K. (2013), Evaluations of SWEs and SPH numerical modelling techniques for dam break flows, Engineering Applications of Computational Fluid Mechanics, 7(4), 544-563.

Ren, B., He, M., Dong, P., Wen, H. J. (2015), Nonlinear simulations of wave-induced motions of a freely floating body using WCSPH method, Applied Ocean Research, 50, 1-12.

Rogers, B.D., R.A. Dalrymple, P.K. Stansby. Simulation of caisson breakwater movement using 2-D SPH. 2010. Journal of Hydraulic Research, 48, Extra Issue, 135-141.

Schwaiger, H. F. (2008), An implicit corrected SPH formulation for thermal diffusion with linear free surface boundary conditions. International Journal for Numerical Methods in Engineering, 75, 647-671.

Shao, S., Lo, E.Y.M. (2003), Incompressible SPH method for simulating Newtonian and non-Newtonian flows with a free surface, Advances in Water Resources, 26, 787-800.

Shao, S. (2005), SPH simulation of solitary wave interaction with a curtain-type breakwater, Journal of Hydraulic Research, 43(4), 366–375.

Zheng, X., Ma, Q. W., Duan, W. Y. (2014), Incompressible SPH method based on Rankine source solution for violent water wave simulation, Journal of Computational Physics, 276, 291-314.